American Mineralogist, Volume 91, pages 1432–1441, 2006

EXAFS signature of structural Zn at trace levels in natural and synthetic trioctahedral 2:1 phyllosilicates

FARID JUILLOT,[1,*] GUILLAUME MORIN,[1] PHILIPPE ILDEFONSE,[1,†] GEORGES CALAS,[1] AND GORDON E. BROWN, JR.[2,3]

[1]Institut de Minéralogie et de Physique des Milieux Condensés (IMPMC), UMR CNRS 7590, Universités Paris 6 et 7, IPGP, Campus Boucicaut, 75015 Paris, France

[2]Surface and Aqueous Geochemistry Group, Department of Geological and Environmental Sciences, Stanford University, Stanford, California 94305-2115, U.S.A.

[3]Stanford Synchrotron Radiation Laboratory, SLAC, 2575 Sand Hill Road, MS 69, Menlo Park, California 94025, U.S.A.

ABSTRACT

EXAFS spectroscopy has been used to determine the medium-range structural environment (within a radius of ≈7 Å) of trace levels of Zn^{2+} ions within the octahedral sheets of trioctahedral 2:1 phyllosilicates. EXAFS signatures of trace quantities (800–4000 ppm) of Zn in natural and synthetic trioctahedral 2:1 phyllosilicates (talcs and biotite) were analyzed using ab initio FEFF calculations (FEFF 8.10 code) in which various second-neighbor atomic configurations around a Zn-containing octahedral site were examined. Comparison of the results of these model calculations with observed Zn *K*-edge EXAFS spectra provides constraints on the distribution of Zn within the octahedral sheet. Zn was found to be randomly distributed within the octahedral sheets of the synthetic talc containing 4000 ppm Zn. In the natural biotite containing 800 ppm Zn, the distribution of Zn could not be determined because of significant Fe content, which precluded unambiguous FEFF analysis. Finally, FEFF analysis of single-scattering and multiple-scattering contributions to the EXAFS data of the Zn-dilute talc sample, followed by comparison with EXAFS data from a natural dioctahedral illite sample containing 140 ppm Zn, allowed unambiguous identification of spectral features characteristic of Zn^{2+} ions incorporated within the octahedral sheets of trioctahedral phyllosilicates. These results indicate that EXAFS spectroscopy can be used to distinguish between incorporation of trace levels of Zn^{2+} ions within the octahedral sheet of di- or trioctahedral phyllosilicates. They also provide a strong basis for determining the speciation of Zn at trace concentration levels in natural phyllosilicates from Zn-contaminated soils and sediments using Zn *K*-edge EXAFS spectroscopy. Because the crystal chemistry of other potentially toxic first-row divalent transition elements (i.e., Co^{2+}, Ni^{2+}, and Cu^{2+}) is similar to that of Zn^{2+}, this FEFF-based EXAFS approach could be used to (1) complement existing FTIR and polarized-EXAFS approaches in assessing the distribution of these elements within the octahedral sheets of di- and trioctahedral plyllosilicates and (2) better determine the speciation of these elements in contaminated soils and sediments.

Keywords: Zinc, phyllosilicates, EXAFS, FEFF, trace levels

INTRODUCTION

Recent investigations of Zn-contaminated soils have renewed interest in the local structural environments of Zn^{2+} ions in di- and trioctahedral phyllosilicates and other layered structures of environmental relevance (Manceau et al. 2000; Roberts et al. 2002; Scheinost et al. 2002; Voegelin et al. 2002; Juillot et al. 2003). Zn^{2+} can form end-members or non-ideal solid solutions with Mg^{2+} in trioctahedral phyllosilicates (see, e.g., Brindley and Brown 1980; Bailey 1988 and references therein), as illustrated by the smectite group minerals sauconite (the Zn end-member) and stevensite (the Mg end-member), which form a complete solid solution (Ross 1946; Faust 1951). Zn-rich talcs have been synthesized by Wilkins and Ito (1967), and sauconites have been synthesized at 80 °C by Decarreau (1981, 1983, 1985). The serpentine-group minerals zinalsite, the Zn-amesite end-member (Wicks and Whittaker 1975), and baumite, a Zn-rich greenalite, (Frondel and Ito 1975), have also been reported. In addition, baileychlore, a Zn-chlorite end-member, was reported by Rule and Radke (1988). The occurrence of structural Zn^{2+} in dioctahedral phyllosilicates is poorly documented in comparison to the available literature on Zn^{2+} incorporation in trioctahedral layered minerals in spite of the fact that the former are the dominant clay minerals in soils and sediments. As such, they are likely hosts of Zn^{2+} and other divalent cations released from the breakdown of primary Zn-containing minerals. In contrast, the slow kinetics of crystallization of 2:1 dioctahedral phyllosilicates at room temperature likely hinder the incorporation of Zn^{2+} ions within these phases during the time frame of historical pollution events, which do not typically exceed one century at most sites polluted by anthropogenic release of Zn. In Zn-impacted soils, anthropogenic Zn should therefore be more closely associated with trioctahedral phyllosilicates, whereas Zn-bearing dioctahedral phyllosilicates should represent most of the pool of Zn related

* E-mail: juillot@impmc.jussieu.fr
† Deceased October 26, 1999

to the geochemical background resulting from natural weathering processes. Better understanding of Zn behavior in impacted soils would benefit from the ability to (1) distinguish between Zn in di- or trioctahedral phyllosilicates and (2) evaluate the relative chemical stabilities of Zn-bearing di- and trioctahedral phyllosilicates.

These two goals are difficult to achieve because of the similarity of local structures around cations in the octahedral sheets of di- or trioctahedral phyllosilicates and because of the fact that the chemical stability of phyllosilicates is related to the distribution of cations within both the tetrahedral and octahedral sheets. Attenuated total reflectance Fourier transform infrared spectroscopy in the OH-stretching region has been successfully employed to assess the distribution of major elements such as Al, Mg, and Fe in the di- or trioctahedral sheets of phyllosilicates (Slonimskaya et al. 1986; Besson et al. 1987; Madejova et al. 1994; Muller et al. 1997; Besson and Drits 1997a, 1997b; Drits et al. 1997; Vantelon et al. 2001; Petit et al. 2004). However, this method has a low sensitivity to trace elements. In contrast, EXAFS spectroscopy is sensitive to trace levels of cations (>100 ppm) in silicates and has been successfully employed to investigate the distribution of trace levels of Fe and Ni in di- and trioctahedral phyllosilicates (Manceau and Calas 1985, 1986; Manceau 1990; Manceau et al. 1990; Drits et al. 1997; Muller et al. 1997; Vantelon et al. 2003).

The main objective of the present study was to investigate the crystal chemistry of Zn at trace levels in selected synthetic and natural trioctahedral phyllosilicates (synthetic talcs and natural biotite). Because of the low Zn content of the samples investigated (as low as 800 ppm), EXAFS spectroscopy was used to obtain information about the local structural environment of Zn. Ab initio FEFF 8.10 calculations were used to model experimental Zn *K*-edge EXAFS spectra of Zn-dilute talc and biotite samples. Changes in the EXAFS spectra of Zn-bearing phyllosilicates are discussed with respect to Zn concentration and the nature (di- or tri-) of the octahedral sheets. Particular attention was paid to Zn ordering in the trioctahedral sheets to try to distinguish between ordered vs. randomly distributed Zn^{2+} ions.

Materials and methods

Samples studied

The natural trioctahedral phyllosilicate sample selected for this study is a Zn-bearing biotite (800 ppm Zn) from an unknown locality. Crystals exhibit a platey habit; formula calculated from ICP analyses of ground separate crystals is $K_{0.95}Na_{0.02}(Mg_{2.21}Fe_{0.52}Al_{0.10}Ti_{0.09}Mn_{0.02}Zn_{0.005})(Si_{2.78}Al_{1.22})O_{10}(OH)_2{\cdot}nH_2O$ (Table 1).

The mineral purity of the sample used in this study (hereafter referred to as biotite:Zn) was confirmed by X-ray diffraction analyses. For comparison, a Zn-dilute talc sample (4000 ppm Zn), referred to as talc:Zn, and a Zn-end-member talc sample, referred to as Zn-talc, were synthesized following the method of Decarreau (1983). Initial precipitates were prepared by reacting 50 mL of a starting solution of $Zn(NO_3)_2{\cdot}4H_2O$ and $Mg(NO_3)_2{\cdot}6H_2O$ with 200 mL of a 0.1 *M* Na_2SiO_4 solution and 10 mL of a 0.1 *M* HCl solution. The concentrations of the starting solutions were 0.29 *M* $Mg(NO_3)_2{\cdot}6H_2O$ + 0.01 *M* $Zn(NO_3)_2{\cdot}4H_2O$ and 0.3 *M* $Zn(NO_3)_2{\cdot}4H_2O$ for the talc:Zn, and Zn-talc samples, respectively. For each sample, the precipitate was then centrifuged, washed two times with deionized water (milli-Q) and air-dried. Air-dried precipitates were then suspended in deionized water at a concentration of 5 g/L and aged for 21 days at 200° C under vapor pressure in steel autoclaves coated with Teflon. Following these procedures, the chemical composition of talc samples calculated from EPMA analyses are $(Mg_{2.98}Zn_{0.02})Si_4O_{10}(OH)_2{\cdot}nH_2O$ and $Zn_3Si_4O_{10}(OH)_2{\cdot}nH_2O$, for talc:Zn and Zn-talc, respectively.

Phase purity of the natural and synthetic samples studied was checked by powder X-ray diffraction (XRD), counting 20 s per 0.04° 2θ step in the 3° to 80° 2θ range on a Philips PW1730 diffractometer using Co*K*α radiation (40 kV, 30 mA).

Prior to spectroscopic investigations, all samples were reacted for 2 h in a 0.4 *M* HNO_3 solution to remove any surface Zn species or any Zn ions incorporated in miscellaneous Fe- or Mn-oxides that could have been present as trace mineral impurities undetected by XRD. This treatment was followed by cation exchange with a 1 *M* $CaCl_2$ solution for 2 h, to remove any possible Zn^{2+} ions sorbed by electrostatic forces onto mineral surfaces. After each treatment, solids were washed three times with 40 mL of deionized water (milli-Q) and centrifuged at 2800 g after each wash. The solids were then air-dried for spectroscopic investigations.

EXAFS spectroscopy

Zn *K*-edge EXAFS experiments were performed on wiggler beamline IV-3 at the Stanford Synchrotron Radiation Laboratory (SSRL, California, U.S.A.) using a Si(220) double-crystal monochromator. A Pt-coated mirror was used for harmonic rejection above 10 keV. Data were recorded at temperatures of 10–20 K in an Oxford Instruments liquid helium cryostat in the fluorescence detection mode, using a Canberra high-throughput 13-element Ge array detector. The I_0 ion chamber detector was filled with nitrogen gas. Samples were loaded in Teflon sample holders covered with 0.25 mil thickness Kapton tape windows and dunked into liquid nitrogen prior to putting them into a sample cryostat. Slits before the monochromator were set at 2 mm vertically and 20 mm horizontally, and slits after the monochromator were set at 2 mm vertically and 10 mm horizontally so as to avoid the X-ray beam striking the cryostat windows and the sample holder. Energy was calibrated with a Zn metal foil placed after the second ion chamber, with the Zn *K*-edge inflection point chosen to be 9659 eV. For the synthetic Zn-talc and talc:Zn (4000 ppm Zn) samples, two and three scans of 30 min each were accumulated, respectively. For the biotite:Zn sample (800 ppm Zn), 20 scans of 30 min each were accumulated. A Cu (3T) filter was used to attenuate elastic scattering at the Zn *K*-edge for all samples. For the biotite:Zn sample, an additional three absorption length thickness V metal filter was used to attenuate high levels of Fe fluorescence from the sample matrix.

Raw fluorescence spectra were analyzed using standard procedures (see Juillot et al. 2003 for details). E_0 was set at the edge of the inflection point (i.e., at 9663 ± 1 eV) for all samples studied. In a first step, the background contribution before the Zn *K* edge was simulated using a linear function and subtracted from each raw spectrum. In a second step, a spline function with external knots was removed from the post-edge part of each background-subtracted fluorescence spectrum using the XAFS program (Winterer 1997). Each resulting EXAFS spectrum was then Fourier transformed from k space to real space to yield a radial distribution function (RDF) around the central Zn. A Kaiser window between about 2.5 and 12 $Å^{-1}$ with a Bessel weight of 2.5 was used for this latter operation.

Shell-by-shell fitting

For each EXAFS spectrum, first- and second-neighbor contributions in the RDF were back-transformed together by Fourier filtering to yield partial EXAFS spectra arising from these two contributions. Least-squares fitting of these filtered

Table 1. Chemical composition of the natural biotite sample studied

	Biotite:Zn
(wt%)	
SiO_2	38.90
Al_2O_3	15.70
Fe_2O_3	9.74
MnO	0.26
MgO	20.78
CaO	0.02
Na_2O	0.14
K_2O	10.40
TiO_2	1.62
P_2O_5	0.09
L.O.I.	1.38
Total	99.0
(mg/kg)	
Zn	800

Notes: Data from the Centre de Recherches Petrographiques et Geochimiques (CRPG Nancy, France). After fusion with $LiBO_2$ followed by dissolution in HNO_3, major elements and Zn concentrations were determined by ICP-AES and ICP-MS, respectively. L.O.I. = Loss On Ignition.

k^3-weighted EXAFS $\chi(k)$ functions was performed using the plane-wave formalism with a Levenberg-Marquard minimization algorithm. Theoretical phase-shift and amplitude functions employed in this fitting procedure were calculated using the ab-initio FEFF 8.10 code (Ankudinov et al. 1998). Zn-O, Zn-Mg, and Zn-Si phase-shift and amplitude functions were extracted from FEFF calculations on the talc structure [$Mg_3Si_4O_{10}(OH)_2 \cdot nH_2O$, Perdikatsis and Burzlaff 1981] by substituting Zn for the central Mg atom.

FEFF calculations

Theoretical ab initio calculations of Zn *K*-edge EXAFS spectra for Zn in the octahedral sheet of trioctahedral phyllosilicates were performed with the FEFF 8.10 computer code (Ankudinov et al. 1998) on atom clusters of 8 Å in radius, using neither a self-consistent potential nor full multiple-scattering calculations. Based on a trial-and-error approach, the criterion for retaining single-scattering (SS) paths (NLEG 2, i.e., a central Zn-neighbor path and its way back) and multiple-scattering (MS) paths (NLEG 3, i.e., a central Zn-neighbor 1 path, followed by a neighbor 1-neighbor 2 path and a neighbor 2-central Zn path, NLEG 4, NLEG 5, and NLEG 6) was finally reduced down to 1.5% (see FEFF 8.10 documentation) to account for most of the MS paths which significantly contribute to the EXAFS spectrum, and which were observed in the experimental data. MS paths with more than 6 legs (NLEG 6) were found to be negligible, and the total number of scattering paths was between approximately 500 and 1200, depending on the mineral investigated. A Debye temperature of 400 K and an experimental temperature of 10 K were used as input parameters for all calculations and simulate well the attenuation factors observed in the experimental spectra. All calculations were given a constant shift of +8 eV relative to the Fermi level to fit experimental EXAFS spectra. By contrast to the classical shell-by-shell fitting procedure described in the previous paragraph, the present ab initio FEFF calculations consisted in simulating the experimental data without any automatic fitting procedure.

The atomic clusters were built using the structural parameters of Perdikatsis and Burzlaff (1981) for talc samples and those of Brigatti et al. (1991) for the biotite sample. For Zn-dilute samples (talc:Zn and biotite:Zn), a Zn-Mg_6 cluster was constructed by replacing only the central Mg by Zn in the corresponding structure. This first calculation was used to model Zn atoms isolated in the trioctahedral sheets. Other clusters based on the Zn-$[Fe/Zn]_xMg_{6-x}$ formula were also considered to assess the effect of neighboring Fe/Zn around a central Zn ion within the trioctahedral sheets of the samples studied. For the Zn-rich talc sample (Zn-talc), all Mg positions were filled with Zn and a scaling factor of 1.015 was applied to cell parameters to adjust Zn-neighbor distances found by shell-by-shell analyses to obtain the best agreement with experiment. This scaling factor reflects slight local relaxation related to differences in ionic radii between Mg^{2+} and Zn^{2+} in octahedral coordination (0.720 and 0.745 Å, respectively; Shannon 1976). Final spectra for trioctahedral phyllosilicates were computed by a linear combination of 1/3 and 2/3 of the spectra calculated with the central Zn at M1 and M2 sites, respectively. Such a linear combination simulates a random distribution of Zn among the M1 and M2 sites. Other spectra were calculated with various models simulating preferential occupation of the M1 or M2 site by Zn and did not significantly differ from those obtained with the random model. As a consequence, the random Zn model was chosen to investigate the influence of local Zn concentration on the experimental EXAFS spectra of the studied trioctahedral phyllosilicates.

Ab initio calculations of Zn *K*-edge EXAFS spectra for Zn^{2+} ions located in the octahedral sheet of the talc structure, before and after its transformation to a proxy for a M1-vacant dioctahedral 2:1 structure, were also performed using either SS or MS paths. Results of these calculations were used to demonstrate the usefulness of EXAFS spectroscopy to distinguish between incorporation of Zn^{2+} ions within the octahedral sheets of di- or trioctahedral phyllosilicates. The progressive transformation of the talc structure to a proxy for a M1-vacant dioctahedral 2:1 phyllosilicate during these calculations was done as follows. First, a FEFF file was generated with the ATOMS code using the structure of talc (Perdikatsis and Burzlaff 1981), with Mg at one of the two equivalent M2 sites as the central atom. The central Mg was replaced by Zn in the FEFF input file. This FEFF file was then hand-transformed from a trioctahedral to a dioctahedral configuration by removing all of the octahedral cations located in the M1 sites. This resulted in a proxy for a M1-vacant dioctahedral 2:1 structure, i.e., a Zn-Mg_3 cluster, which is reported to be the most probable configuration for illite, for instance (Drits et al. 1998; Sainz-Diaz et al. 2001). Remaining Mg atoms were then replaced by Al to yield a Zn-Al_3 cluster, which is more relevant for simulating Zn incorporation within a dioctahedral 2:1 phyllosilicate.

RESULTS

Shell-by-shell fitting

The k^3-weighted Zn *K*-edge EXAFS data of the three samples studied are presented in Figure 1A, their corresponding radial distribution functions (RDFs) are shown in Figure 1B, and results of the shell-by-shell fitting are shown in Figure 1C. These results are consistent with structural models in which Zn^{2+} cations are incorporated in the octahedral sheets of the studied 2:1 phyllosilicates. In each phyllosilicate sample investigated, Zn is sixfold-coordinated by oxygen with an average Zn-O distance of 2.08 ± 0.02 Å (Table 2). The second-neighbor shell consists of a Zn-Mg contribution at 3.00 ± 0.04 Å, corresponding to edge-sharing octahedra within the trioctahedral sheets, and a Zn-Si contribution at 3.22 to 3.29 ± 0.04 Å, corresponding to corner-sharing $Zn(OH)_6$ octahedra and SiO_4 tetrahedra.

The number of second-neighbors around Zn obtained from the EXAFS fitting is systematically smaller than the theoretical values (Table 2) because of phase cancellations, which are classically observed in the EXAFS spectra of phyllosilicates (Bonnin et al. 1985; Manceau and Calas 1985; Manceau et al. 1988). Indeed, the contribution of the Zn-Mg pair correlation at 3.0 ± 0.04 Å to the EXAFS spectrum is out-of-phase with that of the Zn-Si pair correlation at 3.3 ± 0.04 Å (Fig. 2a). As a consequence, the number of both Mg and Si second-neighbors is underestimated. The number of Mg second-neighbors is only 2.5 (instead of 6) in the trioctahedral sheets of talc:Zn. Likewise, the number of Si second-neighbors is 0.5 (instead of 4) in talc:Zn. The cancellation effects are very strong in the case of talc:Zn due to the presence of 6 Mg second-neighbors which cause cancellation of the EXAFS signal arising from the 4 Si second-neighbors. For the biotite:Zn sample, which contains approximately 1 Fe and 5 Mg per unit cell, the contribution from the Zn-Fe pair correlations is out of phase with that of the Zn-Mg pair correlation (Fig. 2b). As a consequence, the EXAFS signal arising from 5 Mg second-neighbors is cancelled by the EXAFS signal arising from the 1 Fe, and a good fit is obtained with only 2.3 Mg instead of the 5 and 1.7 Si instead of 4.

FEFF calculations

Influence of the nature (single vs. multiple) of the scattering paths. Figures 3, 4, and 5 compare the results of FEFF

TABLE 2. Structural data on the local environment of Zn in the natural and synthetic trioctahedral phyllosilicates samples studied

	First shell (Zn-O)			Second shell (Zn-Cation)			
	R (Å)	N	σ (Å)	R (Å)	N	σ (Å)	ΔE_0(eV)
Zn-talc	2.08	4.6	0.07	3.11	4.8 Zn	0.07	3.0
				3.32	3.3 Si	0.07	
Talc:Zn	2.08	4.3	0.07	3.03	2.5 Mg	0.04	5.6
				3.26	0.5 Si	0.04	
Biotite:Zn	2.08	5.3	0.08	3.03	2.3 Mg	0.05	4.1
				3.29	1.7 Si	0.05	

Notes: The data were obtained from shell-by-shell analysis of the EXAFS data. N is the EXAFS-derived coordination number (accuracy of ±20% for undistorted 1st-neighbors shell), R is the interatomic distance (accuracy of ± 0.02 Å for the average Zn-O distance and ± 0.04 Å for Zn-Cation distances), and σ (Å) is the Debye Waller factor. ΔE_0 (eV) values are referenced to metallic Zn.

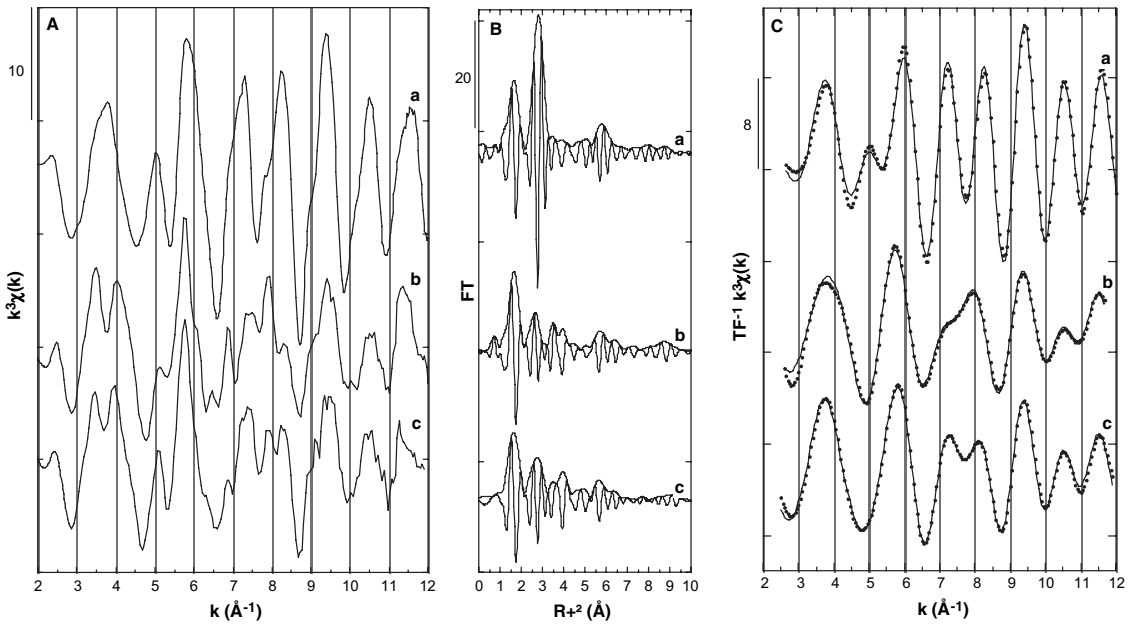

FIGURE 1. Zn *K*-edge $k^3\chi(k)$ functions, RDFs and EXAFS fits of (Aa, Ba, Ca) Zn-talc end-member, $Zn_3Si_4O_{10}(OH)_2 \cdot nH_2O$; (Ab, Bb, Cb) Zn-dilute talc containing ≈ 4000 ppm Zn, $(Mg_{2.98}Zn_{0.02})$ $Si_4O_{10}(OH)_2 \cdot nH_2O$ and (Ac, Bc, Cc) biotite:Zn containing 800 ppm Zn, $K_{0.95}Na_{0.02}$ $(Mg_{2.21}$ $Fe_{0.52}Al_{0.10}Ti_{0.09}Mn_{0.02}Zn_{0.005})(Si_{2.78}Al_{1.22})O_{10}(OH)_2 \cdot nH_2O$. Fits were performed on the Inverse Fourier Transform of the two first shells of the RDFs (solid lines = experimental; dotted lines = calculated).

calculations with experimental EXAFS data from Zn-talc, talc:Zn, and biotite:Zn, respectively. Good matches are obtained for the three EXAFS spectra and RDFs, provided that appropriate multiple-scattering paths are accounted for.

For talc:Zn and biotite:Zn, the agreement between experimental and calculated spectra supports the proposed structural model in which Zn^{2+} cations randomly occupy M1 and M2 sites within the trioctahedral sheets. The EXAFS spectra of Zn-dilute trioctahedral samples (talc:Zn and biotite:Zn) exhibit more detailed features, but with lower magnitude than that of Zn-talc end-member (Figs. 3A, 4A, and 5A). A dramatic increase of the second-neighbor contribution in the RDF (peak B), and the disappearance of the third, fourth, and seventh peaks (referred to as peaks C, D, and G in the RDF of talc:Zn and biotite:Zn) are observed in going from Zn-dilute trioctahedral samples (talc:Zn and biotite:Zn) to the Zn-talc end-member (Figs. 3B, 4B, and 5B). In addition, peak F occurs at a shorter distance for talc:Zn and biotite:Zn than for Zn-talc. Based on FEFF calculations, these complex spectral features can be assigned to single-scattering (SS) and multiple-scattering (MS) paths between the central Zn^{2+} and its surrounding second-neighbor cations within the octahedral sheet and between the octahedral and tetrahedral sheets. These features are detailed in Table 3 and are discussed below.

Zn-talc end-member: FEFF calculations for Zn-talc (Fig. 3B, Table 3), indicate that peak A arises from Zn-O SS paths within the $Zn(O,OH)_6$ octahedra. Peak B arises mainly from Zn-Zn SS paths between edge-sharing $Zn(O,OH)_6$ octahedra, which are reinforced by in-phase Zn-Si SS paths between corner-sharing $Zn(O,OH)_6$ octahedra and SiO_4 tetrahedra from the associated siloxane cavity (Fig. 2B). A small contribution from a long Zn-O SS path (3.40 Å) between corner-sharing $Zn(O,OH)_6$ octahedra and the two nearest SiO_4 tetrahedra from the associated siloxane cavity is also related to this peak (Table 3). Peak E is due to Zn-Zn SS paths between non-adjacent $Zn(O,OH)_6$ octahedra within the sheet. Comparing NLEG 3 and NLEG 2 calculations clearly shows that SS paths dominate the contribu-

TABLE 3. Major SS and MS paths (in angstroms) contributing to the different peaks on the RDFs of natural and synthetic trioctahedral phyllosilicates samples studied

	Zn-Talc	Talc:Zn	Biotite:Zn
Peak A	Zn-O @ 2.05	Zn-O @ 2.05	Zn-O @ 2.05
	Zn-Zn @ 3.10	Zn-Mg @ 3.05	Zn-Mg/Fe @ 3.05
	Zn-Si @ 3.30	Zn-Si @ 3.25	Zn-Si @ 3.25
Peak B	Zn-O @ 3.40*	Zn-O @ 3.35*	Zn-O @ 3.40*
		Zn-O-Si @ 3.50	Zn-O-Si @ 3.50
		Zn-O-Mg @ 3.55	Zn-O-Mg/Fe @ 3.60
		Zn-O @ 3.70	Zn-O @ 3.70
Peak C		Zn-O @ 4.05	Zn-O-O @ 4.10
		Zn-O-O @ 4.10	Zn-O @ 4.15
		Zn-O-O @ 4.40	Zn-O-O @ 4.35
		Zn-Si @ 4.45	Zn-Si @ 4.50
Peak D		Zn-O-Si @ 4.45	Zn-O-Si @ 4.65
		Zn-O @ 4.55	Zn-O-O @ 4.60
		Zn-O-O @ 4.60	Zn-O @ 4.70
Peak E	Zn-Zn @ 5.35		
	Zn-Zn @ 6.20	Zn-Si-O @ 6.00	Zn-Mg-Mg @ 6.10
Peak F	Zn-Zn-Zn @ 6.20	Zn-Mg-Mg @ 6.10	Zn-Mg-Mg-Mg @ 6.10
	Zn-Zn-Zn-Zn @ 6.20	Zn-Mg-Mg-Mg @ 6.10	Zn-O-Si @ 6.15
		Zn-O @ 6.75	Zn-O-O @ 6.75
Peak G		Zn-O-O @ 6.75	Zn-O-K @ 6.80
			Zn-K @ 6.80*
			Zn-Si-K @ 6.85

Note: All paths, except those labeled with a star, are mean paths between two or more similar paths within a range of 0.2 Å.

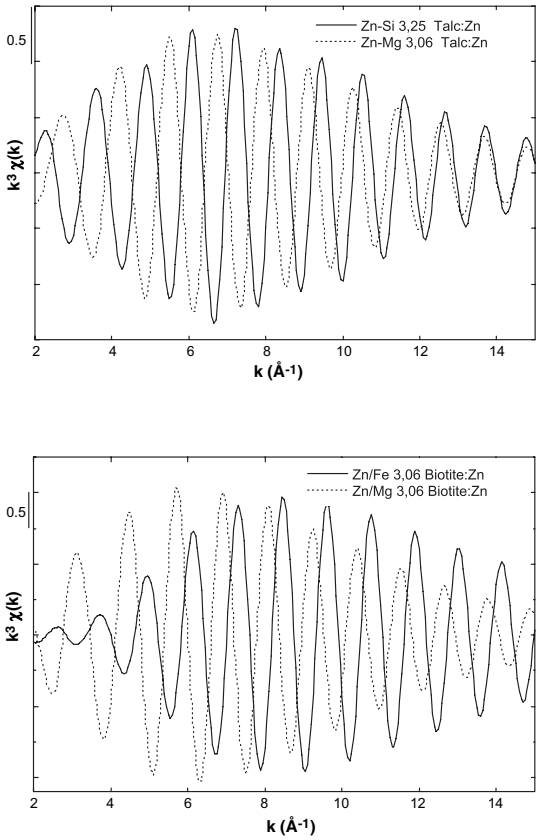

FIGURE 2. FEFF calculated partial Zn *K*-edge $k^3\chi(k)$ functions for (**a**) Zn-Si and Zn-Mg paths in talc:Zn, and (**b**) Zn-Fe and Zn-Mg paths in biotite:Zn.

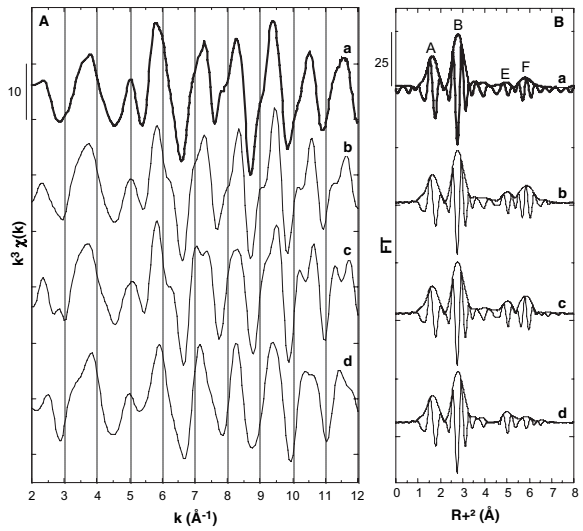

FIGURE 3. Comparison of Zn *K*-edge (A) $k^3\chi(k)$ functions and (B) RDFs of (**a**) experimental Zn-talc with FEFF-calculated Zn *K*-edge EXAFS data using (**b**) NLEG 6, (**c**) NLEG 3 and (**d**) NLEG 2 SS and MS paths.

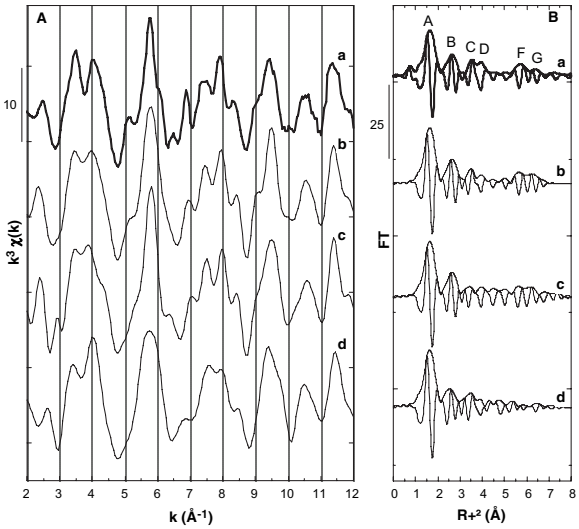

FIGURE 4. Comparison of Zn *K*-edge (A) $k^3\chi(k)$ functions and (B) RDFs of (**a**) experimental talc:Zn with FEFF-calculated Zn *K*-edge EXAFS data using (b) NLEG 6, (**c**) NLEG 3 and (**d**) NLEG 2 SS and MS paths.

tions to these three RDF peaks (Figs. 3Bc and 3Bd, Table 3). Peak F also includes a small contribution from Zn-Zn SS paths between non-adjacent $Zn(O,OH)_6$ octahedra, but "3-leg" Zn-Zn-Zn and "4-leg" Zn-Zn-Zn-Zn focusing MS paths between collinear edge-sharing $Zn(O,OH)_6$ octahedra mainly contribute to its magnitude (Table 3).

Zn-dilute talc: For talc:Zn (Fig. 4B, Table 3), peak A arises from Zn-O SS paths within $Zn(O,OH)_6$ octahedra. Peak B is located at a shorter apparent distance than for Zn-talc because of the larger phase-shift for the Zn-Mg pair than for the Zn-Zn pair. The NLEG 2 calculation shows that half of the magnitude of this peak arises from the combination of Zn-Mg SS paths between edge-sharing $Zn(O,OH)_6$ and $Mg(O,OH)_6$ octahedra with out-of-phase Zn-Si SS paths between corner-sharing $Zn(O,OH)_6$ octahedra and the two nearest SiO_4 tetrahedra from the associated siloxane cavity. A long Zn-O SS path (3.35 Å) between the corner-sharing $Zn(O,OH)_6$ octahedra and the two nearest SiO_4 tetrahedra from the associated siloxane cavity also contributes to this peak (Table 3). The NLEG 3 calculation shows that the other half of the magnitude of peak B comes mainly from Zn-O-Mg MS paths between edge-sharing $Zn(O,OH)_6$ and $Mg(O,OH)_6$ octahedra, and Zn-O-Si MS paths between corner-sharing $Zn(O,OH)_6$ octahedra and SiO_4 tetrahedra defining the associated siloxane cavity(Table 3). Peaks C and D both arise from "3-leg" Zn-O-O MS contributions between edge-sharing $Zn(O,OH)_6$ and $Mg(O,OH)_6$ octahedra, and Zn-O-Si MS contributions between corner-sharing $Zn(O,OH)_6$ octahedra and SiO_4 tetrahedra from the associated siloxane cavity. However, the main contributors to these peaks are long Zn-O (up to 4.55 Å) and Zn-Si (up to 4.45 Å) SS paths between $Zn(O,OH)_6$ octahedra and SiO_4 tetrahedra from the associated siloxane cavity (Table 3). Peak F arises primarily from "3-leg" Zn-Mg-Mg and "4-leg" Zn-Mg-Mg-Mg MS focusing paths between collinear edge-sharing $Zn(O,OH)_6$ and $Mg(O,OH)_6$ octahedra. At such long distances, the contribution from Zn-Mg SS paths from non-adjacent $Zn(O,OH)_6$ and

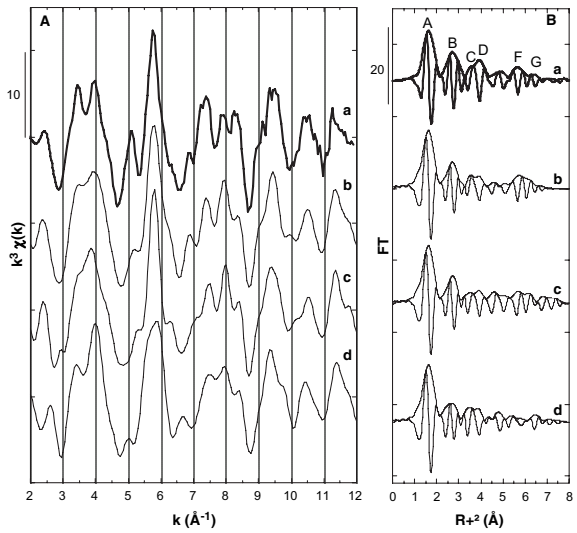

FIGURE 5. Comparison of Zn *K*-edge (A) $k^3\chi(k)$ functions and (B) RDFs of (**a**) experimental biotite:Zn with FEFF-calculated Zn *K*-edge EXAFS data using (**b**) NLEG 6, (**c**) NLEG 3, and (**d**) NLEG 2 SS and MS paths.

$Mg(O,OH)_6$ octahedra is negligible compared to that of Zn-Zn SS paths found in Zn-talc. Peak G comes from both Zn-O SS paths between $Zn(O,OH)_6$ octahedra and SiO_4 tetrahedra from the associated siloxane cavity, and "3-leg" Zn-O-O, "4-leg" Zn-O-O-O, and "5-leg" Zn-O-Zn-O-O MS paths, either within $Zn(O,OH)_6$ octahedra or between $Zn(O,OH)_6$ octahedra and SiO_4 tetrahedra from the associated siloxane cavity.

Zn-dilute biotite: For biotite:Zn (Figs. 5A and 5B, Table 3), FEFF calculations indicate that the positions of all features observed in the experimental EXAFS spectrum and in the corresponding RDF could be reproduced with SS paths, but that MS paths were necessary to obtain their correct relative amplitudes. Assignment of the RDF peak is similar to that in talc:Zn. Peak A in the RDF is related to short Zn-O SS paths within $Zn(O,OH)_6$ octahedra. SS paths related to peak B are mainly Zn-Mg, Zn-Fe, Zn-Si, and long Zn-O (3.40 Å) SS paths between edge-sharing $Zn(O,OH)_6$ and $Mg(O,OH)_6$ octahedra and corner-sharing $Zn(O,OH)_6$ octahedra and the two nearest SiO_4 tetrahedra from the associated siloxane cavity (Table 3). This peak also comes from Zn-O-Mg MS paths between edge-sharing $Zn(O,OH)_6$ and $Mg(O,OH)_6$ octahedra, and to Zn-O-Si MS paths between corner-sharing $Zn(O,OH)_6$ octahedra and the two nearest SiO_4 tetrahedra from the associated siloxane cavity (Table 3). Peaks C and D arise mainly from long Zn-O (up to 4.70 Å) and Zn-Si (up to 4.50 Å) SS paths between corner-sharing $Zn(O,OH)_6$ octahedra and SiO_4 tetrahedra from the associated siloxane cavity (Table 3). As for Talc:Zn, "3-leg" Zn-O-O MS paths between edge-sharing $Zn(O,OH)_6$ and $Mg(O,OH)_6$ octahedra and Zn-O-Si MS paths between corner-sharing $Zn(O,OH)_6$ octahedra and SiO_4 tetrahedra also contribute to this peak (Table 3). Peak F arises from "3-leg" Zn-Mg-Mg and "4-leg" Zn-Mg-Mg-Mg focusing MS paths between collinear edge-sharing $Zn(O,OH)_6$ and $Mg(O,OH)_6$ octahedra. Peak G is related to both Zn-O SS paths between $Zn(O,OH)_6$ octahedra and SiO_4 tetrahedra from the associated siloxane cavity, and "3-leg" Zn-O-O, "4-leg" Zn-O-O-O, and "5-leg" Zn-O-Zn-O-O MS paths, either within $Zn(O,OH)_6$ octahedra or between $Zn(O,OH)_6$ octahedra and SiO_4 tetrahedra from the associated siloxane cavity. In contrast with talc:Zn, additional Zn-K SS paths, and "3-leg" Zn-Si-K and Zn-O-K MS paths including K ions in the interlayer position also contribute to peak G (Table 3).

Influence of the nature (light vs. heavy) of the cations occupying the second-neighbor shell around Zn^{2+} ions. FEFF calculations with the central Zn^{2+} ion surrounded by Mg^{2+} cations or by a mixture of Mg^{2+} and Zn^{2+}/Fe^{2+} cations in the trioacthedral sheets of Zn-dilute talc and biotite samples indicate that the *k* region in the Zn EXAFS spectrum between 7 and 9 $Å^{-1}$ is very sensitive to the composition of the second-neighbor shell around a central Zn (Figs. 6 and 7). The same observation was made by Scheinost and Sparks (2000), who applied the FEFF 7.02 code to distinguish among Ni/Al-LDH, layered Ni hydroxide, and Ni-containing phyllosilicates. Because of this sensitivity, FEFF calculations can be used to assess the number and types of Zn second-neighbor cations within the octahedral sheets of the phyllosilicates studied.

Zn-dilute talc: In the synthetic talc:Zn sample, comparison of FEFF-calculated and experimental EXAFS spectra showed that the EXAFS spectrum calculated with only second-neighbor Mg^{2+} cations around a central Zn is a good match with the experimental spectrum (Figs. 6a and 6b). FEFF calculations assuming one or more Zn^{2+} ions in the second-neighbor shell did not reproduce the experimental EXAFS spectrum, as illustrated in Figures 6c and 6d for $Zn\text{-}Zn_1Mg_5$, and $Zn\text{-}Zn_2Mg_4$ clusters.

Zn-dilute biotite: In the natural biotite:Zn sample, a FEFF calculation based on a $Zn\text{-}Mg_6$ cluster matches the experimental spectrum of biotite:Zn reasonably well, but it failed to accurately reproduce the relative amplitudes of the features in the *k*-range 7–9 $Å^{-1}$ (Figs. 5A and 7b). In contrast, a calculation including one Fe/Zn in the second-neighbor shell around a central Zn [i.e., a $Zn\text{-}(Fe/Zn)_1Mg_5$ cluster] yielded the correct relative amplitudes of the features in the *k*-range 7–9 $Å^{-1}$ (Fig. 7c). Adding more than one Fe/Zn in this shell yields changes in the calculated EXAFS spectrum that do not agree with the experimental spectrum, as is shown for a $Zn\text{-}(Fe/Zn)_2Mg_4$ cluster (Fig. 7d). Because Fe and Zn have similar electron backscattering amplitudes, distinction between these two cations is not possible with EXAFS spectroscopy in this case.

Influence of the nature (di- vs. tri-) of the octahedral sheet. Figures 8A and 8B compare the RDFs of FEFF calculations for Zn^{2+} ions incorporated within the octahedral sheet of a Zn-dilute talc, before and after its transformation to a proxy for a M1-vacant dioctahedral 2:1 structure, with experimental EXAFS data from trioctahedral talc:Zn. A good match is obtained between calculation and experiment only with the initial trioctahedral structure and when appropriate MS paths are accounted for (Figs. 8Ab and 8Ac). If the talc structure is transformed to a proxy for the M1-vacant dioctahedral structure , FEFF calculations cannot reproduce peak F, and the intensity of peak B is strongly decreased, even when MS paths are considered (Figs. 8Bb and 8Bc). These results are in agreement with the fact that peak F arises from a combination of "3-leg" Zn-Mg-Mg and "4-leg" Zn-Mg-Mg-Mg MS focusing paths between collinear

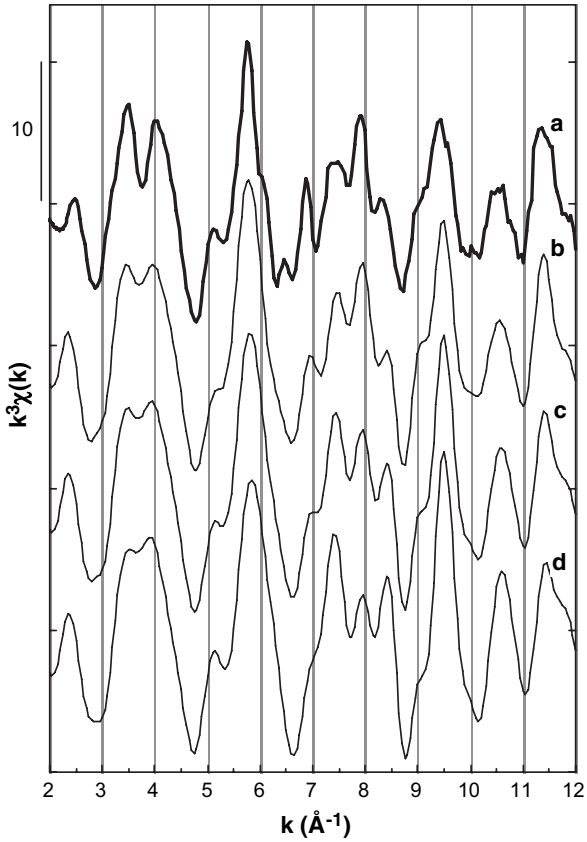

FIGURE 6. Comparison of (**a**) experimental and (**b**, **c**, and **d**) FEFF-calculated Zn *K*-edge EXAFS data for talc:Zn. FEFF calculations with (**b**) Zn-Mg_6, (**c**) Zn-Zn_1Mg_5, and (**d**) Zn-Zn_2Mg_4 clusters show the influence of Zn occupancy in the second-neighbor shell around central Zn.

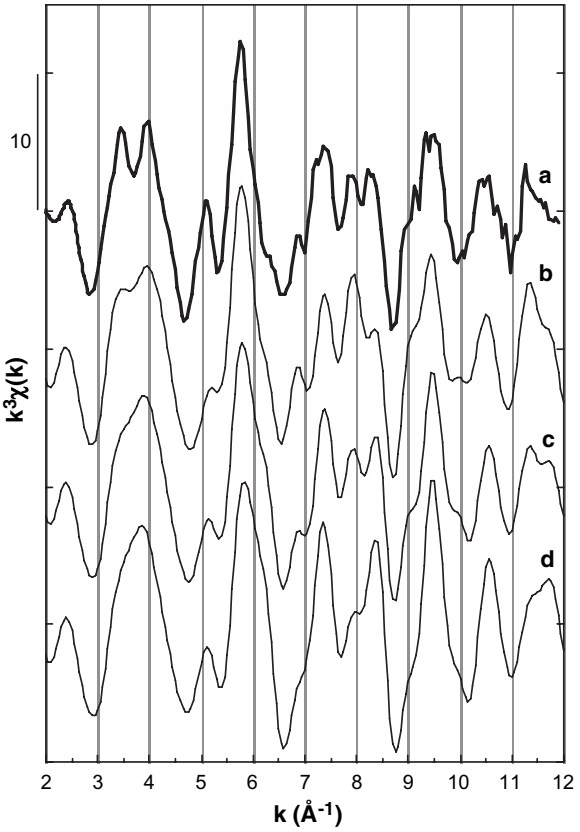

FIGURE 7. Comparison of (**a**) experimental and (b, c, and d) FEFF-calculated Zn *K*-edge EXAFS data for biotite:Zn. FEFF calculations with (**b**) Zn-Mg_6, (**c**) Zn-Fe_1Mg_5, and (**d**) Zn-Fe_2Mg_4 clusters show the influence of Fe occupancy in the second-neighbor shell around central Zn.

edge-sharing $Zn(O,OH)_6$ and $Mg(O,OH)_6$ octahedra. When M1 cations are removed from the initial trioctahedral talc structure to yield a proxy for a M1-vacant dioctahedral 2:1 structure, such MS processes can no longer occur, and peak F does not appear in the FT of the EXAFS data. Peak G is observed in the FEFF-calculated RDfs with the talc structure transformed to a proxy for a M1-vacant dioctahedral 2:1 structure because MS paths related to this peak occur between $Zn(O,OH)_6$ octahedra and SiO_4 tetrahedra from the associated siloxane cavity and thus are not dependent on the focusing effect.

DISCUSSION

Comparison of experimental and FEFF-calculated Zn EXAFS spectra of the phyllosilicates considered in this study allowed us to distinguish between possible atomic models of the local environment of Zn^{2+} ions, including the local concentration of this element and the nature (di- or tri-) of the octahedral sheets. We first discuss changes in the EXAFS spectra of synthetic talc and natural biotite samples with respect to Zn concentration in the trioctahedral sheets. This is followed by a discussion of the distribution of Zn in trioctahedral sheets of these phyllosilicates. Finally, the influence of the nature (di- or tri-) of the octahedral sheets on the EXAFS spectra is discussed based on a comparison of FEFF calculations for tri- and dioctahedral sheets.

Effect of Zn concentration on the EXAFS spectrum of Zn^{2+} in the octahedral sheets of trioctahedral 2/1 phyllosilicates

Differences between the EXAFS spectra of the Zn-dilute trioctahedral samples (talc:Zn and biotite:Zn) and that of the Zn-talc end-member reflect changes in local Zn concentration, which are expected from the different total Zn concentrations in the three samples. Several peaks in the RDFs can be used to distinguish between high and low Zn concentrations in the local vicinity of the central Zn atom probed by EXAFS (Figs. 3, 4, and 5). Peak B is the most sensitive to Zn concentration because of the large contribution of SS paths between adjacent $Zn(O,OH)_6$ octahedra in the Zn-talc end-member, or between adjacent $Zn(O,OH)_6$ and $Mg(O,OH)_6$ octahedra in the Zn-dilute samples (talc:Zn and biotite:Zn). Because of the higher electron backscattering amplitude of Zn compared to Mg, the larger the number of Zn^{2+} cations in the trioctahedral sheets, the higher the magnitude of this peak. Peaks C and D are only observed in the RDF of the Zn-dilute samples (talc:Zn and biotite:Zn). As discussed earlier, these peaks are mainly due to long Zn-O and Zn-Si SS paths between corner sharing $Zn(O,OH)_6$ octahedra and SiO_4 tetrahedra. These paths are not clearly observed in the RDF of Zn-talc end-member mainly because their contribution is small with respect to that of the strong Zn-Zn contributions from adjacent octahedra.

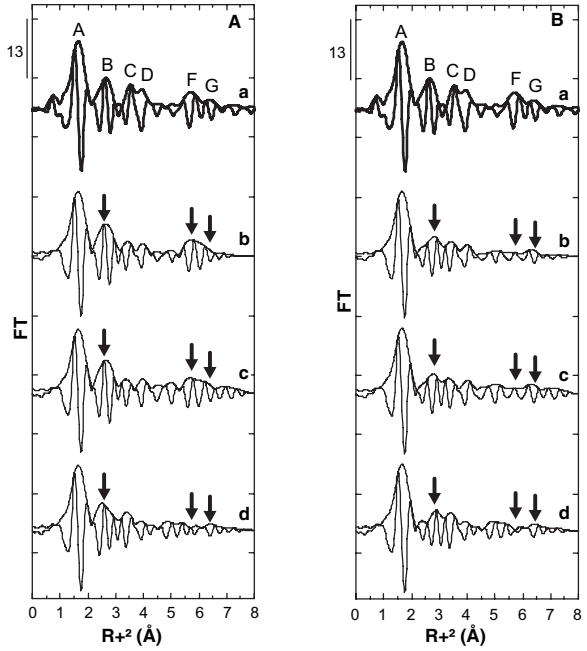

FIGURE 8. Comparison of experimental Zn *K*-edge RDFs of (**a**) talc:Zn with FEFF-calculated Zn *K*-edge EXAFS data of (A) initial talc structure from Perdikatsis and Burzlaff (1981) with central Zn at M2 site and (B) M1-vacant talc structure with central Zn at M2 site used as a proxy for dioctahedral 2:1 phyllosilicate. For each cluster, FEFF calculations were performed either with (**b**) NLEG 6, (**c**) NLEG 3, or (**d**) NLEG 2 SS and MS paths.

Local distribution of Zn^{2+} ions in the octahedral sheet of Zn-dilute trioctahedral 2/1 phyllosilicates

The distribution of cations within the octahedral sheets of phyllosilicates can be assessed by comparing their average second-neighbor environment derived from EXAFS analysis with the average environment calculated from the structural formula assuming a random distribution. Observed deviations from a random distribution indicate either clustering or maximum separation of cations. Considering a random distribution of a cation M, the probability of finding various local cluster configurations can be assessed by a binomial law of the following form:

$$P_k = C_n^k x^k (1\text{-}x)^{n-k} \quad (1)$$

where P_k, n, and x are, respectively, the probability of finding k M cations adjacent to a central atom, the number of adjacent sites, and the concentration of the M cation with respect to the total number of sites (e.g., x = number of M per cell/Σ number of octahedral cations per cell). Using this formalism, we can examine the relative distribution of Zn with respect to Mg, Al, and Fe within the octahedral sheets of the samples studied, as discussed below.

Zn-dilute biotite. In the synthetic biotite:Zn sample, where Zn is present at a minor level (800 ppm Zn), the binomial law can be applied to assess the Zn local environment in the case of a random distribution of this element over all octahedral sites. Assuming such a random distribution, the low Zn concentration (800 ppm wt. Zn; $x_{Zn} = 0.0017$) in the biotite:Zn sample yields a very low probability ($1 - P_{k=0} = 0.01$) of finding adjacent Zn (pairs + trimers + others) around a central Zn, according to Equation 1. However, the significant Fe concentration of biotite:Zn [chemical formulae derived from EPMA is $K_{0.95}Na_{0.02}(Mg_{2.21}Fe_{0.52}Al_{0.10}Ti_{0.09}Mn_{0.02}Zn_{0.005})(Si_{2.78}Al_{1.22})O_{10}(OH)_2 \cdot nH_2O$] indicates that an average of one Fe and five Mg should be found in the second-neighbor shell around a central Zn, unless Fe and Zn concentrate in separate areas.

FEFF calculations indicate that each central Zn has, on average, one Fe/Zn atom within its second-neighbor shell (Fig. 7). Adding more than one Fe/Zn in this second-neighbor shell yields changes in the calculated EXAFS spectrum that do not agree with the experimental data. This EXAFS result can be interpreted as being due to either a "random" or an "ordered" distribution of Zn, depending on the distribution of Fe. If Fe is randomly distributed over the octahedral sheets, results of FEFF calculations indicate that Zn is also randomly distributed over all octahedral sites, and the transition element within the second-neighbor shell around central Zn is Fe. If Fe concentrates in specific areas, Zn might be either segregated in Zn-rich clusters within Fe-poor zones or randomly distributed over all octahedral sites, including Fe-rich and Fe-poor regions. The uncertainty about the local distribution of Zn in this Fe-rich biotite sample comes from the fact that Fe and Zn cannot be distinguished by EXAFS spectroscopy because they have similar electron backscattering amplitudes. A first attempt using FTIR in the OH-stretching region to try to assess the distribution of Fe within the octahedral sheets of the Zn-dilute biotite sample was not successful because of the lack of appropriate reference spectra in the literature; further FTIR analyses are in progress.

Zn-dilute talc. As for natural biotite:Zn, the binomial law can also be used to predict the local environment of Zn in the case of a random distribution of Zn over all octahedral sites of the synthetic talc:Zn sample (4000 ppm Zn). According to Equation 1 and considering the Zn concentration (4000 mg/kg) which yields a x_{Zn} value of 0.0067, the probability of finding adjacent Zn (pairs + trimers + others) around a central Zn is $1\text{-}P_{k=0} = 0.04$. This value indicates that if Zn is randomly distributed in the trioctahedral sheets of talc:Zn, 96% of the Zn^{2+} ions should be surrounded by 6 Mg atoms in the second-neighbor shell. FEFF calculations indicated that a Zn-Mg_6 cluster better fits the experimental spectrum than Zn-$Zn_xMg_{6\text{-}x}$ clusters (Fig. 6). This result demonstrates that Zn is surrounded dominantly by Mg and that little if any Zn occurs within the second-neighbor shell of an average Zn^{2+} ion in talc:Zn. This conclusion is consistent with a random distribution of Zn in this sample, according to the binomial law.

The good match between experimental Zn *K*-edge EXAFS spectra of the synthetic Zn-dilute talc samples and ab-initio FEFF-calculated EXAFS spectra for model clusters based on a random distribution of Zn demonstrates that a few thousand ppm of Zn can be randomly incorporated in the octahedral sheets of trioctahedral phyllosilicates. To the best of our knowledge, no other data are available that constrain the local distribution of Zn in clay minerals. However, our results can be discussed in

light of several FTIR and EXAFS studies carried out on other elements such as Fe and Ni. In a recent ATR-FTIR study, Petit et al. (2004) found evidence for a random distribution of Fe in natural talc samples at Fe concentrations ranging from 15 to 0.35 wt% Fe_2O_3, with the lowest concentration sample being similar to that of Zn in our talc:Zn sample. However, our results contrast with previous investigations of Manceau (1990) and Manceau et al. (1990) who concluded that Ni or Fe segregated within the trioctahedral sheets of Ni- or Fe-phyllosilicates. The differences between our results for dilute Zn-phyllosilicates and those of Manceau and co-workers for Ni- and Fe-phyllosilicates could be related to differences in concentration of the divalent cations in the phyllosilicates studied. Indeed, the lowest Ni/(Ni + Mg) and Fe/(Fe + Mg) ratios explored in the studies of Manceau (1990) and Manceau et al. (1990) were 0.04 and 0.06, respectively. These ratios are much higher than the Zn/(Zn + Mg) ratio of 0.007 in the most concentrated of our Zn-dilute trioctahedral sample (talc:Zn), which suggests that divalent cations could be randomly distributed in the trioctahedral sheets of phyllosilicates below a threshold concentration, whereas they would segregate within these sheets above this concentration. However, the results of Petit et al. (2004), which indicate a random distribution of Fe within the trioctahedral sheets of natural talc samples, are also applicable for higher Fe/(Fe + Mg) ratios (0.27) than those of Manceau and co-workers. This difference relative to previous studies emphasizes the fact that other factors in addition to the M/(M + Mg) ratio, especially the temperature of formation, are expected to have a significant influence on the local distribution of cations within the octahedral sheet of clay minerals.

Further work should be undertaken to explore the relative importance of the nature of the cations, the total cation concentration, and the temperature of synthesis on the distribution of divalent cations within octahedral sheets of trioctahedral phyllosilicates, and to determine the impact of these distributions on thermodynamic properties. The FEFF-based approach to EXAFS data analysis used in this study could be very useful for such future studies.

Comparison of EXAFS signals arising from Zn^{2+} ions in Zn-dilute di- or trioctahedral sheets of 2/1 phyllosilicates

The main difference between the EXAFS data for Zn^{2+} ions in the octahedral sheet of Zn-dilute di- and trioctahedral phyllosilicates is the absence of MS peaks around 6 Å in the RDF of dioctahedral phyllosilicates (Figs. 8A and 8B). This difference is due to the fact that vacancies in the dioctahedral sheets hinder the MS focusing effects responsible for these peaks in the trioctahedral sheets, as illustrated by FEFF calculations performed on the trioctahedral talc structure, before and after its transformation to a proxy for a M1-vacant dioctahedral one. This relative importance of MS vs. SS paths contributing to the EXAFS signal of Zn at trace levels in the octahedral sheets of phyllosilicates allows a relatively clear distinction between Zn incorporation within di- or trioctahedral sheets.

The relationship between the peaks around 6 Å in the RDF values of trioctahedral layered minerals and MS paths between collinear edge-sharing $M(O,OH)_6$ octahedra was previously pointed out by O'Day et al. (1994) in Co-layered double hydroxide (Co-LDH) after Co sorption onto kaolinite edge sites (followed by partial dissolution of the kaolinite and co-precipitation of Co-LDH), by Manceau et al. (2000) for Fe in nontronite, and by Trainor et al. (2000) in Zn-LDH after Zn sorption onto the α-Al_2O_3 surface (followed by partial dissolution of alumina and co-precipitation of Zn-LDH). However, in contrast with these previous studies, where the main M cation in collinear edge-sharing $M(O,OH)_6$ octahedra responsible for these MS peaks was Co, Fe, or Zn (i.e., a transition element with strong electron backscattering amplitude), our FEFF analysis based on the structure of trioctahedral talc and biotite indicates that these MS peaks can also be observed when the backscattering M cation in collinear edge-sharing $M(O,OH)_6$ octahedra is a light element (i.e., Mg). These MS peaks should therefore be observed in dilute phyllosilicate samples, assuming the concentration of M cation is sufficient to be detected by electron backscattering in the EXAFS spectrum.

Based on these results, it should be possible to use the occurrence or absence of MS peaks around 6 Å in the RDFs of dilute, or concentrated, phyllosilicates to unambiguously distinguish between M cation incorporation within dioctahedral or trioctahedral sheets of phyllosilicates. This conclusion is a very useful one for studies of contaminated samples containing phyllosilicates or other layered minerals with dilute levels of potentially toxic first-row transition elements (i.e., Co, Ni, and Cu) in which EXAFS MS focusing effects are operative.

ACKNOWLEDGMENTS

This paper is dedicated to Prof. Philippe Ildefonse, our late friend and colleague, who initiated this work on spectroscopic signatures of transition elements at trace levels in phyllosilicates. The authors are indebted to the SSRL staff, especially the SSRL Biotechnology Group, as well as to J.R. Bargar (SSRL) for their technical assistance during the experiments at SSRL. This work was supported by the cooperative CNRS-NSF research program involving the University of Paris VI-VII and Stanford University under grants CNRS-INT-5914 and NSF-INT-9726528, by the European Commission Framework IV Program Grant ENV4-CT97-0554, and by NSF-EMSI Grant CHE-0431425 (Stanford Environmental Molecular Science Institute). This is IPGP contribution no. 2138.

REFERENCES CITED

Ankudinov, A.L., Ravel, B., Rehr, J.J., and Conradson, S.D. (1998) Real space multiple scattering calculation and interpretation of X-ray absorption near edge structure. Physical Review B 58, 7565.

Bailey, S.W. (1988) Hydrous phyllosilicates (exclusive of micas), vol. 19, p. 725. Reviews in Mineralogy, Mineralogical Society of America, Chantilly, Virginia.

Besson, G. and Drits, V.A. (1997a) Refined relationships between chemical composition of dioctahedral fine-grained mica minerals and their infrared spectra within the OH-stretching region. Part I: Identification of the OH-stretching bands. Clays and Clay Minerals, 45, 158–169.

——— (1997b) Refined relationships between chemical composition of dioctahedral fine-grained mica minerals and their infrared spectra within the OH-stretching region. Part II : The main factors affecting OH vibrations and quantitative analysis. Clays and Clay Minerals, 45, 170–183.

Besson, G., Drits, V.A., Daynyak, L.G., and Smoliar, B.B. (1987) Analysis of cations distribution in dioctahedral micaceous minerals on the basis of IR spectrosocpy data. Clay Minerals, 22, 465–478.

Bonnin, D., Calas, G., Suquet, H., and Pezerat, H. (1985) Sites occupancy of Fe^{3+} in Garfield nontronite: a spectroscopic study. Physics and Chemistry of Minerals, 12, 55–64.

Brigatti, M.F., Galli, E., and Poppi, L. (1991) Effect of Ti substitution in biotite-1M crystal chemistry. American Mineralogist, 76, 1174–1183.

Brindley, G.W. and Brown, G. (1980) Crystal structures of clay minerals and their X-ray identification, Mineralogical Society Monograph 5, p. 495. Mineralogical Society, London.

Decarreau, A. (1981) Cristallogénèse à basse température de smectites trioctaédriques par vieillissement de coprécipités silicométalliques. Comptes Rendus de l'Académie des Sciences Paris 292, 61–64 (in French).

——— (1983) Etude expérimentale de la cristallogénèse des smectites. Mesure des coefficients de partage smectite trioctaédrique-solution acqueuse pour les métaux M^{2+} de la première série de transition. Sciences Géologiques 74.

Institut de Géologie, Université Louis pasteur de Strasbourg and CNRS Eds., p. 197 (in French).
——— (1985) Partitioning of divalent transition elements between octahedral sheets of trioctahedral smectites and water. Geochimica et Cosmochimica Acta, 49, 1537–1544.
Drits, V.A., Dainyak, L.G., Muller, F., Besson, G., and Manceau, A. (1997) Isomorphous cation distribution in celadonites, glauconites and Fe-illites determined by infrared, Mössbauer and EXAFS spectrocopies. Clay Minerals, 32, 152–179.
Drits, V.A., Lindgreen, H., Salyn, A.L., Ylagan, R., and McCarty, D.K. (1998) Semiquantitative determination of trans-vacant and cis-vacant 2:1 layers in illites and illite-smectites by thermal analysis and X-ray diffraction. American Mineralogist, 83, 1188–1198.
Faust, G.T. (1951) Thermal analysis and X-ray studies of sauconite and some zinc minerals of the same paragenese association. American Mineralogist, 36, 795–822.
Frondel, C. and Ito, J. (1975) Zinc rich chlorites from Franklin, New Jersey. Neues Jahrbuch für Mineralogie Abhteilung, 123, 111–115.
Juillot, F., Morin, G., Ildefonse, P., Trainor. T.P., Benedetti, M.F., Galoisy, L., Calas, G. and Brown, G.E., Jr. (2003) Occurrence of Zn/Al hydrotalcite in smelter-impacted soils from northern France: Evidence from EXAFS spectroscopy and chemical extractions. American Mineralogist, 88, 509–526.
Madejova, J., Komadel, P., and Cicel, B. (1994) Infrared study of octahedral site populations in smectite. Clay Minerals, 29, 319–326.
Manceau, A. (1990) Distribution of cations among the octahedra of phyllosilicates; Insight from EXAFS. Canadian Mineralogist, 28, 321–328.
Manceau, A. and Calas, G. (1985) Heterogeneous distribution of nickel in hydrous silicates from New caledonia ore deposits. American Mineralogist, 70, 549–558.
——— (1986) Nickel-bearing clay minerals: II. Intracrystalline distribution of nickel : an X-ray absorption study. Clay Minerals, 21, 341–360.
Manceau, A., Bonnin, D., Kaiser, P., and Frétigny, C. (1988) Polarized EXAFS of biotite and chlorite. Physics and Chemistry of Minerals 16, 180–185.
Manceau, A., Bonnin, D., Stone, W.E.E., and Sanz, J. (1990) Distribution of Fe in the octahedral sheet of trioctahedral micas by polarized EXAFS. Physics and Chemistry of Minerals, 17, 363–370.
Manceau, A., Lanson, B., Schlegel, M.L., Harge, J.C., Musso, M., Eybert-Berard, L., Hazemann, J.L., Chataignier, D., and Lamble, G.M. (2000) Quantitative Zn speciation in smelter-contaminated soils by EXAFS spectroscopy. American Journal of Science, 300, 289–343.
Muller, F., Besson, G., Manceau, A., and Drits, V.A. (1997) distribution of isomorphous cations within octahedral sheets in montmorillonite from Camp-Bertaux. Physics and Chemistry of Minerals, 24, 159–166.
O'Day, P.A., Brown, G.E., Jr., and Parks, G.A. (1994) X-ray absorption spectroscopy of cobalt(II) multinuclear surface complexes and surface precipitates on kaolinite. Journal of Colloid and Interface Science, 165, 269–289.
Perdikatsis, B. and Burzlaff, H. (1981) Strukturverfeinerung am talk $Mg_3[(OH)_2Si_4O_{10}]$. Zeitschrift für Kristallographie, 156, 177–186.
Petit, S., Martin, F., Wiewiora, A., De Parseval, P., and Decarreau, A. (2004) Crystal-chemistry of talc: A near infrared (NIR) spectroscopy study. American Mineralogist, 89, 319–326.
Roberts, D.R., Scheinost, A.C., and Sparks, D.L. (2002) Zinc speciation in a smelter-contaminated soil profile using bulk and microspectroscopic techniques. Environmental Science and Technology, 36, 1742–1750.
Ross, C.S. (1946) Sauconite—a clay mineral from the montmorillonite group. American Mineralogist, 31, 411–424.
Rule, A.C. and Radke, F. (1988) Baileychlore, the Zn end-member of the trioctahedral chorite series. American Mineralogist, 73, 135–144.
Sainz-Diaz, C. I., Hernandez-Laguna, A., and Dove, M.T. (2001) Theoretical modelling of cis-vacant and trans-vacant configurations in the octahedral sheet of illites and smectites. Physics and Chemistry of Minerals, 28, 322–331.
Scheinost, A.C. and Sparks, D.L. (2000) Formation of layered single- and double-metal hydroxide precipitates at the mineral/water interface: A multiple-scattering XAFS study. Journal of Colloid and Interface Science, 223, 167–178.
Scheinost, A.C., Kretzschmar, R., Pfister, S., and Roberts, D.R. (2002) Combining selective sequential extractions, X-ray absorption spectroscopy and principal component analysis for quantitative zinc speciation in soil. Environmental Science and Technology, 36, 5021–5028.
Shannon, R.D. (1976) Revised effective ionic radii and systematic studies of interatomic distances in halides and chalcogenides. Acta Crystallographica A, 32, 751–767.
Slonimskaya, M.V., Besson, G., Daynyak, L.G., Tchoubar, C., and Drits, V.A. (1986) Interpretation of the IR spectra of celadonites and glauconites in the region of OH-stretching frequencies. Clay Minerals, 21, 377–388.
Trainor, T.P., Brown, G.E., Jr., and Parks, G.A. (2000) Adsorption and precipitation of aqueous Zn(II) on alumina powders. Journal of Colloid and Interface Science, 231, 359–372.
Vantelon, D., Pelletier, M., Michot, L.J., Barres, O., and Thomas, F. (2001) Fe, Mg and Al distribution in the octahedral layer of montmorillonites. An infrared study in the OH-bending region. Clay Minerals, 36, 369–379.
Vantelon, D., Montarges-Pelletier, E., Michot, L.J., Briois V., Pelletier, M., and Thomas, F. (2003) Iron distribution in the octahedral sheet of dioctahedral smectites. An Fe *K*-edge X-ray absorption spectroscopy study. Physics and Chemistry of Minerals, 30, 44–53.
Voegelin, A., Scheinost, A.C., Bühlmann, K., Barmettler, K., and Kretzschmar, R. (2002) Slow formation and dissolution of Zn precipitates in soil: A Combined column-transport and XAFS study. Environmental Science and Technology, 36, 3749–3754.
Wicks, F.J. and Whittaker, E.J.W. (1975) A reappraisal of the structures of the serpentine minerals. Canadian Mineralogist 13, 227–243.
Wilkins, R.W.T. and Ito, J. (1967) Infrared spectra of some synthetic talcs. American Mineralogist, 52, 1649–1661.
Winterer, M. (1997) XAFS—A data analysis program for materials science. Journal de Physique VI, 7, C2, 243.

MANUSCRIPT RECEIVED FEBRUARY 21, 2005
MANUSCRIPT ACCEPTED MAY 2, 2006
MANUSCRIPT HANDLED BY LEE GROAT